Shock transitions in Marangoni gravity-driven thin-film flow

2000 Nonlinearity 13 731

(http://iopscience.iop.org/0951-7715/13/3/312)

Nonlinearity **13** (2000) 731–746. Printed in the UK PII: S0951-7715(00)06158-2

Shock transitions in Marangoni gravity-driven thin-film flow

Andreas Münch

Zentrum Mathematik, Technische Universität München (H4), D-80290 Munich, Germany

Received 20 July 1999, in final form 3 February 2000
Recommended by G Morriss

Abstract. Thin films of silicon oil driven up an inclined silicon wafer by a thermally induced Marangoni force develop unusual shock profiles involving a non-classical undercompressive shock, if the counteracting parallel component of gravity is sufficiently large (Bertozzi *et al* 1998 *Phys. Rev. Lett.* **81** 5169–72). They arise as a result of the interaction of a non-convex flux with the fourth-order diffusion generated by surface tension. In this work, we investigate how the dynamical behaviour of the solution is affected by including second-order diffusion resulting from the normal component of gravity; this component was neglected in the previous study. Then the governing equation for the film profile $h(x, t)$ becomes

$$h_t + (h^2 - h^3)_x = -(h^3 h_{xxx})_x + D(h^3 h_x)_x \qquad D \geqslant 0.$$

The numerical simulations in this paper confirm that neglecting second-order diffusion is justified for small D, but find that for larger D, the structure of the solution changes dramatically. We give a detailed account of the transitions that occur while increasing D and make predictions for future experiments carried out at small inclination angles, corresponding to moderately large D.

AMS classification scheme numbers: 35L65, 37L67, 35Q35, 37C29, 35K30

1. Introduction

We consider the motion of a thin film of silicon oil driven up an inclined silicon wafer by a thermally induced Marangoni stress. Recent experimental and theoretical work [1, 2] has shown unusual dynamical behaviour of the film profile, with the appearance of non-classical undercompressive shocks [3, 4], for which characteristics pass through the shock trajectory, rather than entering from both sides.

We briefly introduce model equations for the height $h(x, y, t)$ of the film profile. Conservation of mass for the liquid requires

$$h_t + \nabla \cdot (h\boldsymbol{V}) = 0$$

where

$$\boldsymbol{V} = \left(\frac{\tau}{2\eta}h - \frac{\rho g \sin\alpha}{3\eta}h^2\right)\boldsymbol{e}_x - \frac{\rho g \cos\alpha}{3\eta}h^2\nabla h + \frac{\gamma}{3\eta}h^2\nabla\Delta h$$

is a depth-averaged velocity that results from a lubrication approximation (see also [5–7]). Here τ denotes the surface tension gradient, η the viscosity, ρ, g the density and the gravitational constant, γ the surface tension and α the angle of inclination (from the horizontal); $\boldsymbol{e}_x$ denotes the unit vector for the x-axis. Coordinates have been introduced so that x, y are the directions parallel to the plate, with x pointing up the slope and y in the spanwise direction, respectively. In this paper, we seek solutions with no y dependence. Such profiles are of physical relevance

if they are stable with respect to spanwise perturbations, or as base profiles for a stability analysis if they are not.

As in [2], we choose scales H, l, T, for h, x and t, respectively, such that the time derivative, the convective term and the contribution from surface tension balance, i.e. $H = 3\tau/(2\sin\alpha\rho g)$, $l = \left(2\gamma H^2/(3\tau)\right)^{1/3}$ and $T = 2\eta\left(\frac{4}{9}\tau\gamma\rho g\sin\alpha\right)^{1/3}/\tau^2$. This results in the non-dimensionalized equation

$$h_t + f(h)_x = -(h^3 h_{xxx})_x + D(h^3 h_x)_x \tag{1}$$

where f denotes the flux function $f(h) = h^2 - h^3$. The parameter $D = \left(9\tau^2/4\gamma\rho g\right)^{1/3}\cot\alpha/(\sin\alpha)^{1/3}$ measures the relative importance of the normal component of gravity. It is zero for vertical wafers but increases monotonically for decreasing inclination angle; in fact, $D \sim \alpha^{-4/3}$ as $\alpha \to 0$, if the surface tension gradient τ is kept fixed.

We choose boundary conditions consistent with the experiments described in [1]. Far upstream ($x \to -\infty$), the film achieves a uniform thickness h_∞, determined by a meniscus which forms at the surface of the reservoir of silicon oil into which the lower end of the wafer is placed. To model the completely wetting system, we also assume the presence of a thin precursor layer of small thickness $b > 0$, preceding the leading front of the film. A positive b is necessary for (1) to avoid the well known paradox [8, 9] for the case of a moving contact line; see also [7, 10]. Thus we have the boundary conditions

$$\lim_{x\to-\infty} h = h_\infty \qquad \lim_{x\to\infty} h = b. \tag{2}$$

The large-scale, long-time behaviour of (1) and (2) is governed by the lower-order terms in equation (1). To see this, consider for a moment rescaling x and t according to $x' = \epsilon x$, $t' = \epsilon t$. Then, equation (1) becomes (after dropping the primes)

$$h_t + (f(h))_x = -\epsilon^3(h^3 h_{xxx})_x + D\epsilon(h^3 h_x)_x \tag{3}$$

which represents a nonlinear singular perturbation of the *conservation law*

$$h_t + (f(h))_x = 0. \tag{4}$$

Smooth solutions of (4) evolve according to the method of characteristics, but where characteristics cross, shocks form. These are propagating discontinuities, where h jumps from a left value h_- to a right value h_+. In particular, a centred shock wave with propagation speed s is a piecewise constant function

$$h(x,t) = \begin{cases} h_- & \text{if} \quad x < st \\ h_+ & \text{if} \quad x > st. \end{cases} \tag{5}$$

This wave is a weak solution of (4) if the triple (h_-, h_+, s) fulfils the Rankine–Hugoniot condition,

$$s = s(h_+, h_-) = \frac{f(h_+) - f(h_-)}{h_+ - h_-}. \tag{6}$$

The diffusion terms in (1) smooths out the discontinuities to travelling waves, which make the transition from h_- to h_+ over a region of O(1) width.

However, not all discontinuous solutions of (4) actually correspond to a solution of (1); rather, the interaction of the nonlinear flux function with the diffusion terms in (1) determines which shock profiles actually form, in particular, the values of their left and right states $h_\pm$. Moreover, the shock structure may vary for different types of higher-order terms, a fact that we highlight in section 2 by contrasting classical results for the solutions of scalar conservation laws

with second-order viscosity [11] with recently published results [1, 2] for (1) and (2) that focus on pure fourth-order diffusion ($D = 0$). In these recent publications, the authors find that the fourth-order term gives rise to unexpected solutions with an intricate wave structure, involving so-called undercompressive shock profiles, which are not allowed in the classical situation of second-order diffusion; the solutions are found to agree well with thin-film experiments [1]. The comparison of these two extreme cases naturally raises the issue, not considered in the earlier work, of the wave structure for the case of general D, and possible transitions as D is varied. This paper attempts to answer this question, using a combination of numerical and phase space methods.

In section 3, we begin our investigation of general $D \geqslant 0$ with numerical simulations for (1) and (2). In section 4, we explore shock profiles directly, by studying travelling wave solutions $h(\xi)$, $\xi = x - st$ of the partial differential equation (PDE) with the appropriate far-field behaviour ($h \to h_\pm$, and $h' \to 0$, $h'' \to 0$, etc, as $\xi \to \pm\infty$). This amounts to a discussion of heteroclinic orbits for a third-order ordinary differential equation (ODE). In section 5, the results of the previous sections are used to map out the wave structure of the solutions of (1) and (2) in different regions of the parameter space for D, b, h_∞, and to make predictions and suggestions for future physical experiments.

2. Shock structure for second- or fourth-order diffusion

For large $D \gg 1$, we expect second-order diffusion to dominate over the fourth-order term; neglecting the latter, we obtain, after appropriate rescaling,

$$h_t + f(h)_x = (h^3 h_x)_x. \tag{7}$$

The family of shocks which correspond to fronts in solutions of (7) consists of *compressive* or *Lax shocks*, i.e. those shocks that fulfil the Lax entropy condition [11],

$$f'(h_+) < s < f'(h_-) \tag{8}$$

together with *generalized Lax shocks* for which one of the inequalities is an equality. Since $f'(h_\pm)$ is the characteristic speed for the left and right state $h_\pm$ of the shock, respectively, equation (8) requires characteristics from both sides to impinge on the shock trajectory, hence the term 'compressive shock'. Also note that (8) relates the slope of the chord connecting the points $(h_+, f(h_+))$ with $(h_-, f(h_-))$ to the slope of the tangents to the graph of f at these points. Finally, we remark that we obtain a condition equivalent to (8) if we require the chord to lie above the graph of f.

We can now describe the dynamical behaviour of solutions of (7) with boundary conditions (2) and smoothed jump initial data in terms of solutions of (4) satisfying the Lax entropy condition. Within the range of parameters of interest, $0 < b < \frac{1}{3}$ and $h_\infty > b$, we can distinguish two cases, namely, $b < h_\infty < h_m = h_m(b) := (1 - b)/2$ and $h_\infty > h_m$.

(a) If $b < h_\infty < h_m$, the chord connecting $B = (b, f(b))$ and $I = (h_\infty, f(h_\infty))$ lies above the graph of f (see figure 1). In this case, the solution is a single Lax wave.

(b) If $h_\infty < h_m$, the corresponding chord (e.g. from II to B in figure 1) cuts through the graph of the flux function (at I), hence a single shock is not admissible, that is, it does not correspond to a solution of (7) and (2). Instead, a rarefaction–shock evolves,

$$h(x,t) = \begin{cases} h_\infty & \text{if} \quad x < f'(h_-)t \\ (f')^{-1}(x/t) & \text{if} \quad f'(h_-)t < x < f'(h_m)t \\ b & \text{if} \quad x > f'(h_m)t. \end{cases} \tag{9}$$

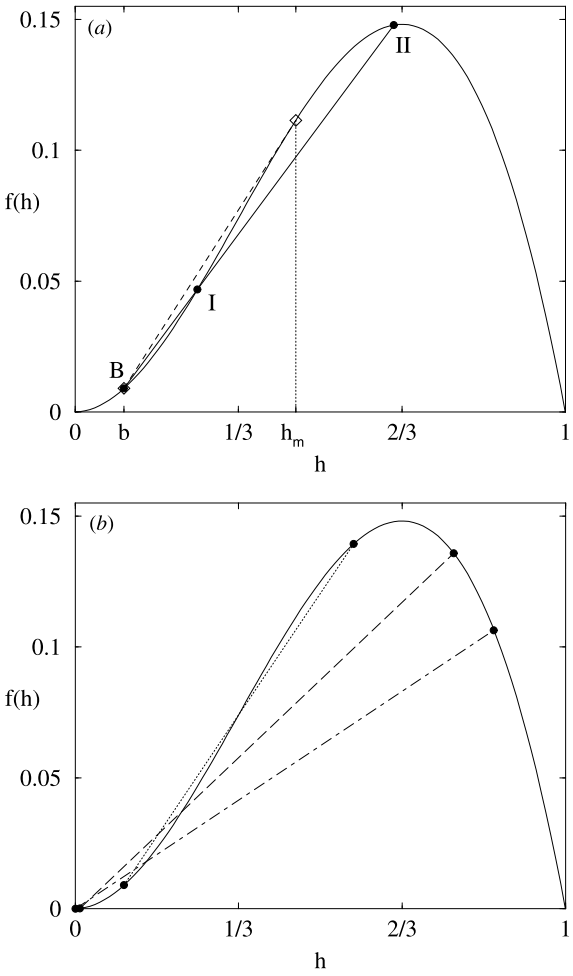

Figure 1. Graphs of the flux function $f(h) = h^2 - h^3$, and chords corresponding to various types of shocks.

The chord corresponding to the leading generalized Lax shock, indicated in figure 1 by a broken line, is tangent at h_m to the graph of f.

In the other limit of (1) with only the fourth-order diffusion term ($D = 0$), the admissible shock structure was investigated in [2], by a combination of numerical simulations of (1) and (2) and phase space investigations for the travelling wave ODE. The authors distinguish four cases.

(a) For $b < h_\infty < h_1(b)$, with a special, b-dependent value h_1, the profile evolves into a single compressive travelling wave.
(b) For $h_1(b) < h_\infty < h_2(b)$, with a second special value h_2, there are several possibilities. Depending on the initial data, the solution evolves to one of multiple travelling waves. All of them correspond to the same compressive shock, but differ in the height of the capillary ridge, or bump, that forms due to the fourth-order smoothing of the jump discontinuity. However, monotonically smoothed jump initial data typically select the travelling wave

with the smallest bump. Within the interval $]h_1(b), h_2(b)[$, there is a further transition at $h_\infty = h_*(b)$. For $h_*(b) < h_\infty < h_2(b)$, and certain smooth jump initial data with a sufficiently large initial bump, one obtains a double wave, consisting of two separating shock profiles. Only the trailing shock fulfils the Lax entropy condition, whereas the leading shock is *undercompressive*, meaning that characteristics pass through its trajectory, rather than entering it from both sides. Here, $h_*(b)$ denotes a third special, b-dependent value in $]h_1(b), h_2(b)[$. The undercompressive shock height $h_{uc}(b)$ is independent of h_∞ and is linked to the other special value by $h_{uc}(b) = 1 - h_*(b) - b$. The chords corresponding to undercompressive shocks cut through the graph of f, as can be seen in figure 1(*b*) for three different value of $b = 0.1$, 0.01 and 0.001 (dotted, broken, chain lines, respectively).

(c) For $h_2(b) < h_\infty < h_{uc}(b)$, the double wave emerges for all smoothed jump initial data.

(d) For $h_\infty > h_{uc}(b)$, the trailing Lax shock in the inviscid limiting solution is replaced by a rarefaction wave, i.e. one obtains a rarefaction–undercompressive shock,

$$h(x,t) = \begin{cases} h_\infty & \text{if} \quad x < f'(h_\infty)t \\ (f')^{-1}(x/t) & \text{if} \quad f'(h_\infty)t \leqslant x < f'(h_{uc})t \\ h_{uc} & \text{if} \quad f'(h_{uc})t \leqslant x < s(h_{uc}, b)t \\ b & \text{if} \quad s(h_{uc}, b)t \leqslant x. \end{cases} \tag{10}$$

Note that, in contrast to the rarefaction–compressive shock combination (9), the leading edge of the rarefaction wave moves at the characteristic speed $f'(h_{uc})$ and hence separates from the undercompressive shock.

3. Numerical simulation for mixed second-/fourth-order diffusion

In this section, we present some results from numerical simulations for (1) and (2) with smoothed jump initial data, where we vary D and h_∞, while keeping b fixed. We observe that the solutions with undercompressive fronts disappear at finite values of D, and are replaced by solutions with the classical shock structure for pure second-order diffusion.

The results in this section were obtained by using a finite-difference scheme discretization of (1) and (2) in space and an implicit Euler scheme for the time integration, see [2, 12] for details.

Figure 2 shows the result of a typical computation, for three different $D = 0, 0.5, 1.5$. The tanh profile

$$h(x,0) = \tfrac{1}{2}\left[(h_\infty + b) + (-h_\infty + b)\tanh(x - x_0)\right] \tag{11}$$

was used as initial data, with $x_0 = 300$, and $b = 0.1$, $h_\infty = 0.425$, and the computations were carried out on a sufficiently long, but finite spatial domain. The results are shown in a frame of reference that moves at the speed $s(h_\infty, b)$ of a simple shock profile connecting h_∞ and b. For the lower two values of D, the figure gives the profiles for each of the solutions at two different times, indicated by broken and full curves, for $t = 2400$ and 4000, respectively.

We see that for $D = 0$ and 0.5, the smooth initial jump evolves into a structure with two fronts that visibly separate, indicating that the corresponding shocks move at different speeds. For both solutions, the speed of both the trailing and the leading front is lower than $s(h_\infty, b)$, and therefore, the fronts appear to move backwards in the figure. Inspection of the corresponding chords in the graph of the flux function reveals that, while the trailing shock profile is compressive, the leading one is undercompressive, since its left state h_{uc} satisfies $h_{uc} > h_m(b) = (1 - b)/2$, implying $s(h_{uc}, b) > f'(h_{uc})$.

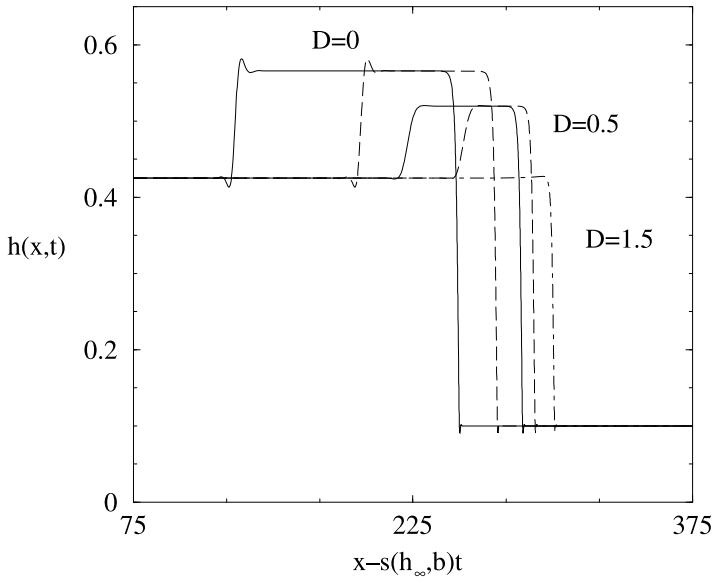

Figure 2. Shock profiles from simulations of (1) and (2) for different values of D, and fixed $b = 0.1$, $h_\infty = 0.425$. For $D = 0, 0.5$, broken and full curves indicate the profiles at $t = 2400$ and 4000, respectively. The chain curve show the simple shock profile that evolves for $D = 1.5$.

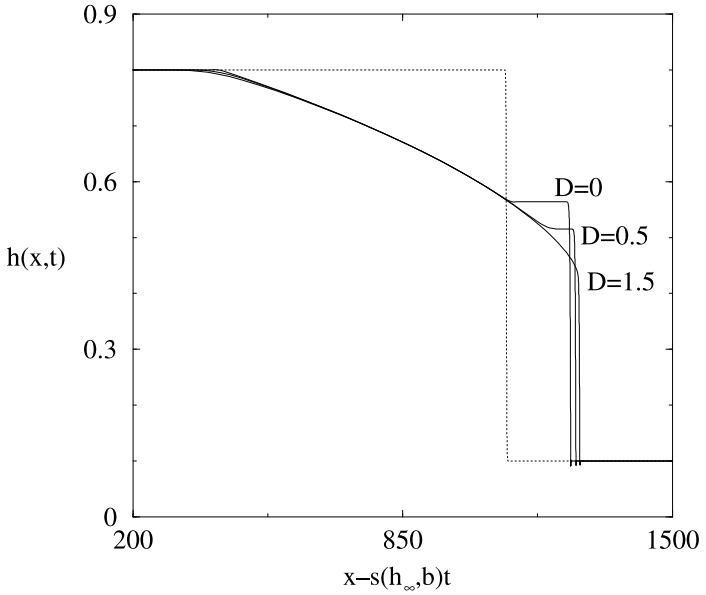

Figure 3. Rarefaction–shock profiles from simulations of (1) and (2) for the same values of D and b as in the previous figure, but $h_\infty = 0.8$. The full curves show the profiles at time $t = 1400$; a dotted line indicates the initial profile used for all three simulations.

The value of h_{uc} depends on D (and b), but not on h_∞. As D is increased, h_{uc} decreases. This increases the slope of the chord connecting the states b and h_{uc}, and hence the velocity of the leading front increases. By comparing the profiles for $D = 0$ and 0.5 in figure 2, or the corresponding chords, one finds that, in addition, the separation rate decreases. For even larger $D = 1.5$, the solution of the initial-value problem converges to a simple compressive wave (chain curve), instead of evolving into a double wave.

For values of $h_\infty > h_m$, rarefaction–shock profiles form in place of the double-shock profiles; in fact, they also occur if, for the given values b and D, $h_\infty > h_{uc}$. Figure 3 shows the result of a simulation for $b = 0.1$ and $h_\infty = 0.8$ and the same three values of D. Again, equation (11) was used as an initial profile (indicated in the figure by a dotted line), with $x_0 = 1000$. For $D = 0, 0.5$, we obtain a rarefaction–undercompressive wave where the leading undercompressive front has the same height h_{uc} as in the corresponding situation, for the same value of D, with a double-shock profile. The leading edge of the rarefaction wave moves with characteristic speed, hence it separates from the undercompressive front. Since $h_{uc} > h_m$ decreases as D is increased, the separation rate $s(h_{uc}, b) - f'(h_{uc})$ decreases as well, as can be seen by considering the corresponding chords in the graph of the flux function. For $D = 1.5$, the rarefaction wave in fact extends right up to the shock, i.e. no separation is observed. This implies that the shock moves at the characteristic speed of its left state, so that for this (and larger) D, we recover the situation of a rarefaction wave connected to a generalized Lax shock that is encountered for pure second-order diffusion.

As a general tendency, we see that our numerical results for larger D are consistent with the classical results for pure second-order diffusion as summarized in section 2, in the sense that undercompressive shock profiles are suppressed for large enough D.

4. Travelling waves

We now investigate the travelling wave solutions $h(\xi)$, $\xi = x - st$ for the PDEs (1) and (2), with $h \to h_\pm$, and $h' \to 0$, $h'' \to 0$, etc, as $\xi \to \pm\infty$. This will give us a complete picture of the transitions of the wave structure, and the precise values for the parameters, in particular for D, at which they occur.

Inserting the travelling wave ansatz into the PDE yields a fourth-order ODE that can be integrated once. The far-field conditions fix the constant of integration and require s to satisfy the Rankine–Hugoniot condition (6), leading to the following third-order ODE for h:

$$h^3 h_{\xi\xi\xi} = Dh^3 h_\xi + (s(h - h_+) - f(h) + f(h_+)). \tag{12}$$

We convert (12) into a first-order system,

$$h' = v \qquad v' = w \qquad w' = Dv + (s(h - h_+) - f(h) + f(h_+))h^{-3} \tag{13}$$

then look for trajectories with the required behaviour at $\xi \to \pm\infty$. Our main focus is on travelling waves that describe the front of the rising film, therefore, we set $h_+ = b$ and assume $h_- \geqslant b$. For (13), we now discuss equilibria, invariant manifolds and orbits connecting equilibria, as we vary the parameters s, b and D.

We first observe that (12) possesses a Lyapunov function

$$L(h) = h''h' + R(h) \qquad \text{with} \quad \frac{\mathrm{d}R(h)}{\mathrm{d}h} = -\frac{s(h - b) - f(h) + f(b)}{h^3}$$

which increases along trajectories, since by differentiating with respect to ξ and using (12) we obtain

$$L(h)' = (h'')^2 + D(h')^2.$$

For a travelling wave connecting h_- and b, it follows that $L(h_-) < L(b)$, hence $R(h_-) < R(b)$. In particular, this rules out the possibility of homoclinic connections.

Equilibria of (13) are given by $(\tilde{h}, 0, 0)$, where $\tilde{h}$ satisfies

$$s(\tilde{h} - b) - f(\tilde{h}) + f(b) = 0. \tag{14}$$

One easily finds the roots for this cubic equation to be

$$\tilde{h}_1 = b \qquad \text{and} \qquad \tilde{h}_{2,3} = h_m(b) \pm \sqrt{f'(h_m(b)) - s} \tag{15}$$

with $\tilde{h}_2$ corresponding to the negative sign in front of the square root. If $s > f'(h_m)$, there is only one real solution for the cubic equation, i.e. only one equilibrium, which is of little use since there can be no homoclinic connections. Furthermore, for the equilibria to be hyperbolic, the three roots have to be distinct, which leads us to require $f'(b) \neq s \neq f'(h_m)$. Finally, equation (14) is also the condition for stationary points of $R(h)$, in fact, for local extrema, since we have restricted the parameter space so that all roots of (14) are simple. The rightmost extremum is necessarily a maximum, since $\mathrm{d}R(h)/\mathrm{d}h \to -1 < 0$ for $h \to \infty$. The remaining extrema $h > 0$ to its left must then be a minimum followed by a maximum, in right-to-left order. From $R(h_-) < R(b)$, it follows that b cannot be the minimum, nor can it be the rightmost maximum, since we have imposed $b < h_-$; therefore, $b < \tilde{h}_2$. This implies $b < \frac{1}{3}$ (since $b + \tilde{h}_2 + \tilde{h}_3 = 1$), and is equivalent to $f'(b) < s$.

Summarizing, we restrict b and s to the range $0 < b < \frac{1}{3}$, $f'(b) < s < f'(h_m(b)$ where, in particular, equation (13) has three distinct equilibria,

$$B = (b, 0, 0) \qquad M = (\tilde{h}_2, 0, 0) \qquad T = (\tilde{h}_3, 0, 0)$$

and seek connections from M to B and M to T.

Linearization of (13) at $I \in \{B, M, T\}$ leads to the characteristic equation

$$\lambda^3 - D\lambda - (s - f'(h_I))h_I{}^{-3} = 0 \tag{16}$$

where h_I refers to the non-zero component of the equilibrium I. We have the possibility of either three real eigenvalues, or a pair of complex-conjugate eigenvalues accompanied by a single real eigenvalue. From Cardano's formula for cubic equations, we see that the latter occurs if and only if

$$\Delta_I(b, s, D) \equiv -\left(\tfrac{1}{3}D\right)^3 + \left(\frac{s - f'(h_I)}{2h_I^3}\right)^2 > 0. \tag{17}$$

For each I, the sum of the eigenvalues is zero, whereas their product is non-zero, since otherwise, $s - f'(h_I) = 0$, which is not possible since our restrictions on b and s ensure that the h_I are simple roots of (14). We conclude that all eigenvalues have a non-zero real part, hence the equilibria are indeed hyperbolic. Moreover, in order for the real parts of the eigenvalues to cancel, exactly two eigenvalues have a real part with the same sign. Since then their product is positive, regardless of whether they are both real or a complex-conjugate pair, the remaining eigenvalue (which is necessarily real) determines the sign of the product of all three eigenvalues. This eigenvalue is therefore positive, or negative, depending on whether $s - f'(h_I) > 0$, or < 0, respectively.

We are now in a position to characterize the stable and unstable manifolds $W^s(I)$ and $W^u(I)$ for all equilibria $I \in \{B, M, T\}$.

- If $s > f'(h_I)$, then $W^u(I)$ is one dimensional and $W^s(I)$ is two dimensional, and vice versa for the opposite inequality. These two cases alternate for equilibria corresponding to consecutive zeros of $s(h-b)-(f(h)-f(b))$. Also, this expression goes to ∞ for $h \to \infty$,

so that the h derivative has to be positive for the topmost zero h_T, i.e. $s - f'(h_T) > 0$. Therefore, T, B have a two-dimensional stable and a one-dimensional unstable manifold, and the converse is true for M.

- Trajectories on the two-dimensional manifold spiral into (or out of) the equilibrium, due to the presence of a complex-conjugate pair of eigenvalues, if and only if $\Delta_I(b, s, D) > 0$.

Orbits connecting M or T to B arise as intersections of the corresponding unstable and stable manifolds. For convenience, these trajectories will sometimes simply be referred to as the 'compressive connections' or 'undercompressive connections', according to the properties of the travelling waves they represent. The orbits from M to B (i.e. the compressive connections, since $s - f'(h_M) < 0 < s - f'(h_B)$) arise as codimension-zero intersections of two two-dimensional invariant manifolds, and hence persist under perturbations of the parameters D, b and s. On the other hand, the connections from T to B (the undercompressive connections, since $s - f'(h_B)$ and $s - f'(h_T)$ are both positive) are codimension-one intersections of a one- and two-dimensional unstable/stable manifold, and generically break under perturbations of the parameters.

Existence of undercompressive connections is established with the following theorem. The proof is given in a recent paper [13].

Theorem 1. *Let $b \in]0, \frac{1}{3}[$. Then there exists a value $D_0 > 0$, so that, for each $D \in [0, D_0]$, there exists a special value $s = s_*(D)$, for which one branch of $W^u(T)$ connects to B, i.e. where we have an undercompressive connection.*

In the same paper, the authors also prove the following complementary result for large D.

Theorem 2. *Let $b \in]0, \frac{1}{3}[$. Then there is a D_1 such that for $D > D_1$ and $f'(b) < s < f'(h_m(b))$, there is no orbit from the equilibrium T to B.*

An example in which both compressive and undercompressive connections are present is shown in the phase portrait of figure 4, for $b = 0.1$, $D = 0$ and $s = 0.278\,588$, with the equilibria lined up along the h-axis, and the one-dimensional unstable manifolds of B and T denoted by dotted curves. The branch of $W^u(T)$ corresponding to the undercompressive connection is emphasized with diamonds. Also indicated are two compressive connections (full curves). The trajectories were computed numerically using an explicit method with step-size control from the LSODE package [14], with initial data close to the respective equilibrium.

Trajectories connecting equilibria can be investigated in a systematic way by looking at the intersections of the stable and unstable manifolds with a Poincaré plane, located, in this paper, at $P = \{h' = -0.05\}$. This choice of P differs from that in [2], where the authors set $P_{old} = \{h = (2h_M + b)/3\}$. The new Poincaré plane was more convenient for larger D, and s close to $f'(h_m(b))$, where the eigenvalues near T are typically real and different from each other. As a consequence, it becomes more difficult to numerically obtain trajectories on $W^u(M)$ very close to $W^u(T)$. This can lead to a visible 'gap' between $W^u(M) \cap P$ and $W^u(T) \cap P$ in the computed Poincaré sections. The gap could be reduced or closed by carrying out the calculations with higher precision (using quadruple-precision arithmetic), which confirms that it is indeed a numerical artefact. Replacing P_{old} with the new P also reduces the gap without using high-precision arithmetic up to the point that it is no longer visible, in the figures shown here.

In the following, b is fixed to be 0.1, while we vary D and s; we remark, however, that the same qualitative picture is obtained for other values of b in $]0, \frac{1}{3}[$. We distinguish three ranges of D.

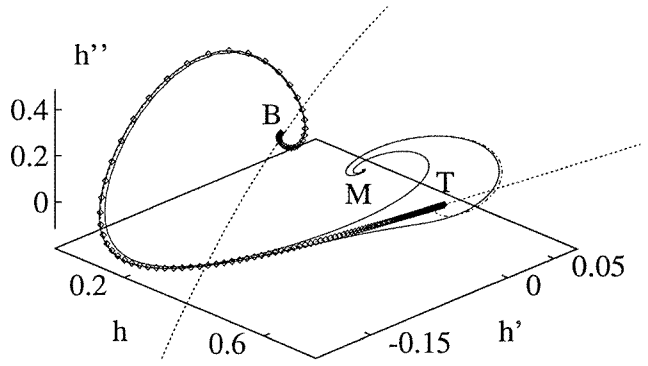

Figure 4. A three-dimensional view of the phase space, for $b = 0.1$, $D = 0$ and $s = 0.278\,588$. Dotted curves indicate $W^u(B)$ and $W^u(T)$. The branch of $W^u(T)$ representing the undercompressive connection from T to B is emphasized by diamonds and the compressive connection from M to B is shown by a full curve. Also indicated is a connection from M to T, by a chain curve.

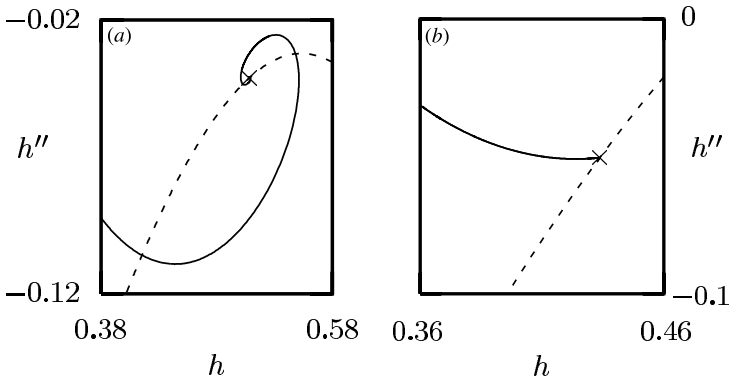

Figure 5. Poincaré sections of the invariant manifolds with the plane $P = \{(h, h', h''); h' = -0.05\}$ for $s = s_*(D)$ and $D = 0$ in (*a*) and $D = 0.9$ in (*b*). The cross shows where $W^u(T)$ intersects with P, whereas full and broken curves represent $W^u(M) \cap P$ and $W^T(M) \cap P$, respectively.

Case I: $0 \leqslant D < D_T$. We find essentially the same situation as reported in [2] for $D = 0$. An undercompressive connection exists for a special speed $s = s_*(D)$. For $D = 0$, we know from the discussion of figure 4 that $s_* = 0.278\,588$, and for this D and s, we obtain the Poincaré section of figure 5. We see that $W^u(T) \cap P$ and $W^s(B) \cap P$ coincide, indicating the existence of an undercompressive orbit. There are also multiple intersections of $W^u(M) \cap P$ and $W^s(B) \cap P$, each representing the place where a compressive orbit crosses the Poincaré plane; hence we have multiple compressive waves.

The spiral structure of $W^u(M)$ is a result of the pair of complex-conjugate stable eigenvalues and the real unstable eigenvalue present in the linearization of the ODE near T. We consider figure 6 for a qualitative description of the situation in phase space, which is not yet rigorous, but suggests that rigorous results can possibly be obtained within the framework of Sil'nikov's method [15]. The cylinder in figure 6 denotes a region in which the vector field near T is approximately linear. The unstable manifold of T is represented by a dotted line, and, for all the orbits depicted, arrows indicate the direction of the flow. Incoming

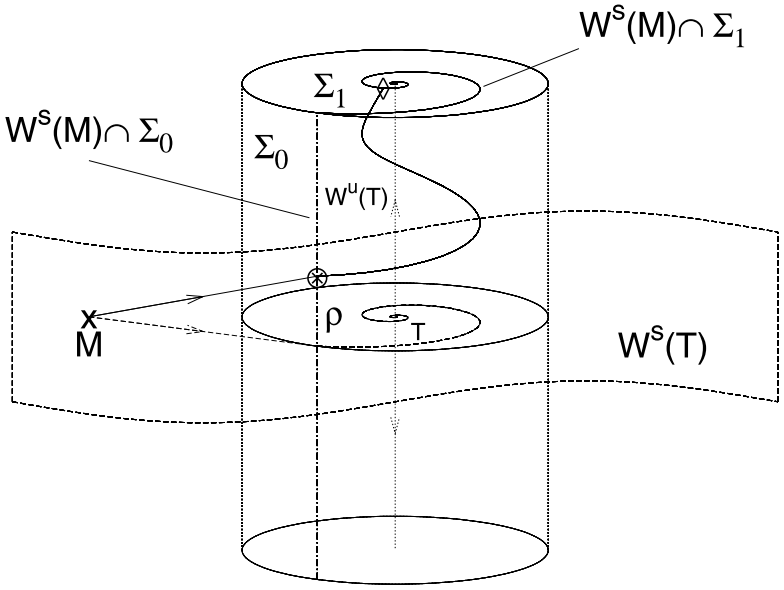

Figure 6. Behaviour of trajectories of $W^s(M)$ that pass near T, for the case where the linearized vector field near T has two complex-conjugate eigenvalues (i.e. $\Delta_T(b, s, D) > 0$).

trajectories from M that cross the cylinder wall Σ_0 are rotated around, and attracted to $W^u(T)$ due to the pair of complex-conjugate stable eigenvalues of T. Except for the connection M to T (broken curve entering a full spiral), which spirals into the equilibrium through an infinite number of windings, the orbits are simultaneously dragged towards the lower or upper lid of the cylinder.

Consider any one of those trajectories which leave through the upper lid Σ_1, and its intersection points S_0 and S_1 with Σ_0 and Σ_1, indicated by $\otimes$ and $\diamond$, respectively. An example of such a trajectory is denoted by a full curve; $W^u(T)$ is represented by a dotted line. The angle formed by S_1 with the projection of S_0 on Σ_1 at $\Sigma_0 \cap W^u(T)$, and the distance of S_1 from the centre of the lid depends on how long the trajectory remains within the cylinder. By the angle we mean the total angle, with multiples of 2π accounting for the windings of the helical structure. Let $\rho \geqslant 0$ be the distance from $W^u(T)$ at which an orbit of $W^u(M) \cap P$ intersects the upper half of Σ_0. In particular, $\rho = 0$ for the intersection of Σ_1 with the orbit connecting M to T. As we decrease ρ to zero, the 'time' the trajectory needs to reach the cylinder lid after passing Σ_0 becomes arbitrarily large. Thus, the distance between S_1 and $W^u(T) \cap \Sigma_1$ decreases arbitrarily, while the aforementioned angle increases arbitrarily. We conclude that, as ρ is varied, the intersection point S_1 moves along a spiral in $W^u(M) \cap \Sigma_1$ centred at $W^u(T) \cap \Sigma_1$, with an infinite number of windings. The numerical results indicate that this spiral structure remains essentially unchanged as we move to a Poincaré plane further away from T.

We now return to the discussion of the Poincaré sections with P for fixed D. If s is increased/decreased above/below $s_*(D)$, respectively, the centre of the spiral shifts to the left or right of $W^s(B) \cap P$. We therefore find three ranges for s, $f'(b) < s < s_1$, $s_1 \leqslant s < s_2$ and $s_2 < s < f'(h_m(b))$, with $s_* \in]s_1, s_2[$, with unique, multiple and no compressive travelling waves, respectively. As s approaches s_* from above or below, a new pair of travelling wave solutions appears each time $W^s(B)$ passes through a new winding of the spiral. In the limit,

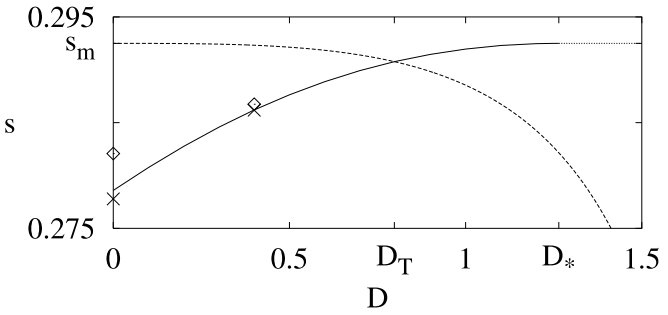

Figure 7. Dependence of the special s on D, for fixed $b = 0.1$. The full curve indicates $s_*(D)$ for $D < D_*$, crosses and diamonds show $s_1(D)$ and $s_2(D)$ for $D = 0$ and 0.4. The broken curve represents $\Delta_T(b, s, D) = 0$.

this cascade of bifurcations leads to an infinite number of compressive connections, with the undercompressive connection at the centre.

Increasing D leaves the qualitative picture intact, as long as we remain within the range of D for which $\Delta_T(b, s_*(D), D)$ (cf equation (17)) is positive. This range is delimited by the value D_T where $\{\Delta_T(b, s, D) = 0\}$, shown in figure 7 by a broken curve, intersects the graph of $s_*(D)$. For $b = 0.1$, this occurs for

$$D_T = 0.797\,85.$$

In figure 7, we see that, as D increases from zero to D_T, $s_*(D)$ increases monotonically. A comparison of $s_2(D) - s_*(D)$ and $s_*(D) - s_1(D)$ for $D = 0$ and 0.4 indicates that both values decrease for increasing D.

Case II: $D_T < D < D_*$. In this range, we still have an undercompressive connection for a special $s = s_*(D)$, but no simultaneous spiral in $W^u(M)$, so we no longer have an infinite number of compressive connections. This range ends by a special value $D_* = \sup\{D;\, s_*(D) < s_m\}$, where the full curve in figure 7 meets $s = s_m \equiv f'(h_m(b))$. For $b = 0.1$, we find D_* to be

$$D_* = 1.2645.$$

Since $\Delta_T(b, s_m, D_*) = -(D_*/3)^3 < 0$, we know that, in general, (D_*, s_m) must lie to the right of the broken curve in figure 7, so that we always have $D_* > D_T$.

A Poincaré section for a value of D just above D_T, and $s = s^*(D) = 0.291\,463$, is given in figure 5(*b*). We see that $W^s(B) \cap P$ and $W^u(M) \cap P$ meet at $W^u(T) \cap P$ at a non-zero angle, suggesting there are no compressive connections. For fixed D, a change in s shifts $W^u(T) \cap P$ with respect to $W^s(B) \cap P$ exactly as before. The structure of $W^s(M) \cap P$ and careful numerical trials for several values of s suggest that we only have to distinguish between two cases for s, namely $s \geqslant s_*(D)$ and $s < s_*(D)$. In the former case, compressive connections are absent, whereas for the latter, there is a unique trajectory from M to B.

Complications could arise in two ways.

(1) If, for $D > D_T$, and for some $s > s_*(D)$, $W^u(M) \cap P$ happens to be strongly curved, a non-empty intersection with $W^s(B)$ could arise. This was never observed, however.
(2) For a range of D above D_T, the spiral in $W^u(M)$, though absent for $s = s_*(D)$, reappears if s is lowered to a range below $s_*(D)$, making multiple intersections possible again,

in principle. However, in all of the cases studied, the spiral was so tightly wound that the distance of its centre from $W^s(B)$ in the Poincaré section was much larger than all the inner windings. Hence, there was only a unique compressive connection, for all $f'(b) < s < s_*(D)$.

We therefore conjecture that the simple picture outlined above correctly describes the situation for $D_T < D < D_*$. Note that this in particular implies that $s_1(D) \to s_*(D)$ and $s_2(D) \to s_*(D)$ as $D \uparrow D_*$.

Case III: $D_* \leqslant D$. In this case, we found $W^u(T) \cap P$ to lie to the right of $W^s(B) \cap P$ in all the Poincaré sections, for all $s \in]f'(b),\ f'(h_m(b))[$. This confirms that undercompressive connections from T to B are not possible in this range of D and s.

5. Consequences for the dynamics

We can now assign specific regions in the (D, h_∞)-parameter space to the different long-time structures observed in the solutions for (1) and (2), in section 3. These regions are shown in figure 8, where they are delimited by different styles of thick curves and full symbols for $b = 10^{-4}$. The corresponding regions for larger values of $b = 0.001, 0.01$ and 0.1 are also indicated by thin curves and open symbols.

In particular, the chain curves shows the left states h_* and h_{uc} of the compressive and undercompressive waves with speed $s = s_*(D)$, i.e. they are given by $h_* = h_M = \tilde{h}_2$, and $h_{uc} = h_T = \tilde{h}_3$, after setting $s = s_*$ in (15). Similarly, $h_1(D)$ and $h_2(D)$ denote the value $\tilde{h}_2$ for $s = s_1(D)$ and $s_2(D)$, respectively. They delimit the hatched area in the figure where multiple compressive connections from M to B exist. We remark that h_1 and h_2 were only

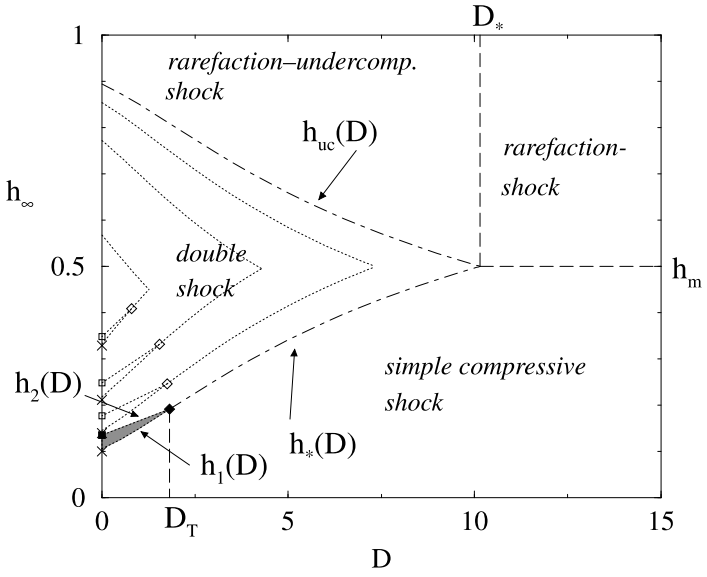

Figure 8. Wave structure of the solution of (1) and (2) that evolves from jump initial data, in different regions of (h_∞, D) parameter space. The thick curves and full symbols correspond to fixed $b = 0.0001$, the thin curves and open symbols correspond to other fixed values of $b = 0.001, 0.01, 0.1$.

calculated for $D = 0$ and set to h_* at $D = D_T$, according to the conjecture in the previous section that $s_1(D)$ and $s_2(D)$ tend to $s_*(D)$ as $D \uparrow D_T$. Approximations of $h_1(D)$ and $h_2(D)$ for other $0 < D < D_T$ were then obtained by interpolation.

For $0 \leqslant D < D_T$, there are essentially the same four ranges for h_∞ as described for the special case of pure fourth-order diffusion ($D = 0$) in section 2. For $D_T < D < D_*$, we have three ranges of h_∞. For $b < h_\infty < h_*(b)$, we obtain a single compressive travelling wave, for $h_*(b) < h_\infty < h_{uc}(b)$, a double-shock profile and for $h_{uc}(b) < h_\infty$, a rarefaction–undercompressive shock profile. As D increases, the ranges of h_∞ with a single compressive travelling wave or a rarefaction–undercompressive shock profile increase at the expense of the range with double fronts. Simultaneously, the height of the undercompressive shock decreases, while its velocity increases. If h_∞ is kept fixed while D is increased, the separation rate of the leading front from the trailing wave (either a compressive shock profile or a rarefaction wave) decreases. Eventually, at $D = D_*$, the values $h_{uc}(D)$ and $h_*(D)$ merge, since, for $D \uparrow D_*$, $s_*(D) \to s_m$. Beyond the critical value D_*, the shock structure of the solution is identical to that of pure second-order diffusion. However, the shock profiles can still have a more or less noticeable capillary ridge for $D > D_*$, as an effect of the fourth-order term.

We finally turn to predictions for future experiments, e.g. for extensions of those reported in [1]. There, the meniscus-controlled thickness of the rising film increased as the inclination angle α was lowered. For thinner films, the experimental profile was that of a simple travelling wave with a capillary ridge of constant height and width. For larger thicknesses, however, the film formed a rather large pronounced bump that continued to broaden until the film left the temperature-controlled zone on the wafer. Furthermore, the rising rates measured for the film front were significantly lower than those expected for a simple travelling wave. Both observations indicate the formation of a double-shock profile with two separating compressive–undercompressive fronts. All these experiments were carried out for values of τ and inclination angles for which $D < \frac{1}{2}$, so that the second-order term could be neglected in [1]. We can now pursue the question of what we can expect to happen, if, for example, α is lowered even further.

An obvious direction to look in experimental observations is the transition in the shock structure at D_*. For a fixed temperature gradient, the critical D_* corresponds to a critical inclination angle α_*. However, even for $b = 0.01$, which is somewhat larger than is adequate for the experiments in [1], D_* is about 4.3, and with typical values for $\tau = 0.18$ Pa, $\gamma = 0.0209$ N m^{-1}, $\rho = 965$ kg m^{-3} reported in the same paper, we obtain $\alpha_* = 2.7^\circ$. This angle is very small and may not be achievable without difficulty in an actual experiment.

If experiments can be designed that allow α to approach the critical value (for example, by increasing b by using wafers with a precoating of silicon oil) the specific observations to be expected depend on how h_∞ is varied with α. In the experimental set-up in [1, 5, 6], the meniscus region at the surface of the reservoir changes with the inclination angle, and so does h_∞, which it controls.

If h_∞ remains below $h_m(b)$ as we increase α (case (a)), a transition to a single travelling wave will eventually occur for some $\hat{D} < D_*$, with $h_\infty = h_*(\hat{D})$ or $h_2(\hat{D})$ at the transition (depending on whether $\hat{D} > D_T$ or $\hat{D} < D_T$, respectively). Let $\hat{\alpha} > \alpha_*$ denote the angle corresponding to $\hat{D}$. The double wave is typically higher than the capillary ridge of the single compressive wave, hence we expect a noticeable decrease in the height of the bump as we pass $\hat{\alpha}$, though the difference tends to be less pronounced if the transition occurs at higher values of $\hat{D}$ (i.e. lower $\hat{\alpha}$). Furthermore, the separation of fronts in the double wave leads to a widening of the bump observed in the experiment, whereas the width of the capillary ridge for a single travelling wave saturates. However, the rate of separation decreases continuously

as α approaches $\hat{\alpha}$, complicating a sharp distinction of double and single waves near the point of transition.

If h_∞ exceeds $h_m(b)$ as we increase α (case (b)), the double-shock profile will first change to a rarefaction–undercompressive wave, which will then gradually become a non-separating classical rarefaction–shock wave as α gets close to α_*. It may therefore be interesting to observe the rate of separation for the rarefaction–shock wave, as α is increased. We note that the rate at which the leading edge of the rarefaction wave separates from the leading undercompressive front is independent of h_∞.

In both cases, the final transition is expected to leave a visible signature in the rising rate of the front. In case (a), the theory predicts rising rates $s(h_{uc}, b) < s(h_\infty, b)$ that tend to $s(h_\infty, b)$ if the transition at $\hat{\alpha}$ occurs with $h_\infty = h_*(\hat{D})$. In case (b), the rising rate of the rarefaction–undercompressive front decreases with α, and then becomes constant for $\alpha \geqslant \alpha_*$.

Even if the critical α_* cannot be approached, a significant impact of the second-order diffusion term on the spreading rate of the leading front can be achieved for somewhat larger α. For values of $b = 0.01$–0.001, a change in D from 0 to about 1.7–1.1, or $\alpha = 5.3^\circ$–7.4° (using the previously mentioned choice for τ, γ and ρ), leads to a change in the undercompressive speed $s_*(D)$ by about 30%. This could be discernible against the uncertainties in the rising rate of the film front visible in the measurements of figure 4 in [1].

Acknowledgments

I thank Andrea Bertozzi, Andrew Bernoff, Anne-Marie Cazabat, Michael Shearer and Barbara Wagner for many helpful discussions. I am especially indebted to Andrea Bertozzi for encouraging me to work on this problem. Some of the work exposed here was done during my stay at Duke University, which was partially supported by ONR grant no N00014-96-0656.

References

[1] Bertozzi A L, Münch A, Fanton X and Cazabat A M 1998 Contact line stability and undercompressive shocks in driven thin film flow *Phys. Rev. Lett.* **81** 5169–72

[2] Bertozzi A L, Münch A and Shearer M 1999 Undercompressive shocks in thin film flow *Physica* D **134** 431–64

[3] Hayes B and Shearer M 1999 Undercompressive shocks and Riemann problems for scalar conservation laws with non-convex fluxes *Proc. R. Soc. Edin.* A **129** 733–75

[4] Shearer M, Schaeffer D G, Marchesin D and Paes-Leme P 1987 Solution of the Riemann problem for a prototype 2×2 system of non-strictly hyperbolic conservation laws *Arch. Rat. Mech. Anal.* **97** 299–320

[5] Carles P and Cazabat A M 1992 On the origin of the bump in the profile of surface-tension-gradient-driven spreading films *Mat. Res. Soc. Symp. Proc.* **248**

[6] Fanton X, Cazabat A M and Quéré D 1996 Thickness and shape of films driven by a Marangoni flow *Langmuir* **12** 5875–80

[7] Kataoka D E and Troian S M 1997 A theoretical study of instabilities at the advancing front of thermally driven coating films *J. Colloid Interface Sci.* **192** 350–62

[8] Dussan E B V and Davis S 1974 On the motion of a fluid–fluid interface along a solid surface *J. Fluid Mech.* **65** 71–95

[9] Huh C and Scriven L E 1971 Hydrodynamic model of steady movement of a solid/liquid/fluid contact line *J. Colloid Interface Sci.* **35** 85–101

[10] Troian S M, Herbolzheimer E, Safran S A and Joanny J F 1989 Fingering instabilities of driven spreading films *Europhys. Lett.* **10** 25–30

[11] Lax P D 1973 *Hyperbolic Systems of Conservation Laws and the Mathematical Theory of Shock Waves* (*CBMS-NSF Regional Conf. Series in Applied Mathematics* vol 11) (Philadelphia, PA: SIAM)

[12] Bertozzi A L and Brenner M P 1997 Linear stability and transient growth in driven contact lines *Phys. Fluids* **9** 530–9
[13] Bertozzi A L and Shearer M 2000 Existence of undercompressive travelling waves in thin film equations *SIAM J. Math. Anal* to be published
[14] Hindmarsh A C 1983 Odepack a systematized collection of ODE solvers *Scientific Computing* ed R S Stepleman *et al* (Amsterdam: North-Holland) pp 55–64
[15] Guckenheimer J and Holmes P 1986 *Nonlinear Oscillations, Dynamical Systems and Bifurcations of Vector Fields* 2nd edn (Berlin: Springer)